Evidence of magnetic mechanism for cuprate superconductivity

2009 New J. Phys. 11 065006

(http://iopscience.iop.org/1367-2630/11/6/065006)

New Journal of Physics
The open-access journal for physics

Evidence of magnetic mechanism for cuprate superconductivity

Amit Keren
Physics Department, Technion-Israel Institute of Technology,
Haifa 32000, Israel
E-mail: keren@physics.technion.ac.il

New Journal of Physics **11** (2009) 065006 (17pp)
Received 27 December 2008
Published 30 June 2009
Online at http://www.njp.org/
doi:10.1088/1367-2630/11/6/065006

Abstract. A proper understanding of the mechanism for cuprate superconductivity can emerge only by comparing materials in which physical parameters vary one at a time. Here, we present a variety of bulk, resonance and scattering measurements on the (Ca_xLa_{1-x}) $(Ba_{1.75-x}La_{0.25+x})$ Cu_3O_y high temperature superconductors, in which this can be done. We determine the superconducting, Néel, glass and pseudopage critical temperatures. In addition, we clarify which physical parameter varies, and, equally important, which does not, with each chemical modification. This allows us to demonstrate that a single energy scale, set by the superexchange interaction J, controls all the critical temperatures of the system. J, in turn, is determined by the in plane Cu–O–Cu buckling angle.

Contents

1. Introduction

The critical temperature for superconductivity T_c in the metallic superconductors Hg, Sn and Tl as a function of $M^{-1/2}$, where M is the atomic mass, is presented in figure 1 on a full scale including the origin [1]. In the case of Sn, a clear isotope effect is observed resulting in a 4% variation of T_c upon isotope substitution. For Hg and Tl, the variations are observed only by zooming in on the data. In all cases, a linear fit goes through the data points and the origin quite satisfactorily, namely, T_c is proportional to $M^{-1/2}$. This observation, known as the isotope effect, plays a key role in exposing the mechanism for superconductivity in metallic superconductors. However, had nature not provided us with isotopes, and we had to draw conclusions only by comparing the different materials in figure 1, we would conclude that T_c has nothing to do with the atomic mass. Thus, figure 1 demonstrates that it is dangerous to compare materials where several quantities vary simultaneously. The isotope experiment overcomes this problem and reveals the origin of metallic superconductivity.

The mechanism for high temperature superconductivity (HTSC) in the cuprate is still elusive, but is believed to be of magnetic origin [2, 3]. Verifying this belief would require an experiment similar to the isotope effect, namely, a measurement of T_c versus the magnetic interaction strength J, with no other structural changes in the compounds under investigation. Unfortunately, varying J experimentally can only be done by chemical variation, usually leading to very different materials. For example, $YBa_2Cu_3O_y$ (YBCO) has a maximum T_c of 96 K, $La_{2-x}Sr_xCuO_4$ has a maximum T_c of 38 K, and both have roughly the same J [4]–[6]. This fact has been used to contradict the magnetic mechanism although these materials are different in crystal perfection, number of layers, symmetry and more. Clearly they are uncomparable exactly as Hg, Sn and Tl.

In the present paper, we describe a set of experiments designed to overcome this problem and to perform a magnetic analog of the isotope experiment by making very small and subtle chemical changes, which modify J but keep all other parameters intact. This is achieved by investigating a system of HTSC with the chemical formula $(Ca_xLa_{1-x})(Ba_{1.75-x}La_{0.25+x})Cu_3O_y$ and acronym CLBLCO. Each value of $x = 0.1, \ldots, 0.4$ is a family of superconductors. All families have the YBCO structure with negligible structural differences; all compounds are tetragonal, and there is no oxygen chain ordering as in YBCO. Within a family, y can be varied from zero doping to over doping.

We present measurements of the critical temperature of superconductivity T_c using resistivity [7], the spin glass (SG) temperature T_g [8] and the Néel temperature T_N [9] of the parent antiferromagnet (AFM) using zero field muon spin relaxation (μSR), the level of doping and the level of impurities by nuclear quadruple resonance (NQR) [10], the superconducting carrier density using transverse field muon spin rotation [11], the lattice parameters, including the oxygen buckling angle, with neutron scattering [12] and the pseudogap (PG) temperature T^* with susceptibility [13]. This allowed us to generate one of the most complete phase diagrams of any HTSC system, to demonstrate a proportionality between T_c and J, and to draw more conclusions.

The paper consists of two main sections in addition to this introduction: in section 2, the main experimental results and parameters extracted from the raw data are presented. In section 3, the conclusions are summarized. Experimental details, raw data and analysis description are given in appendices.

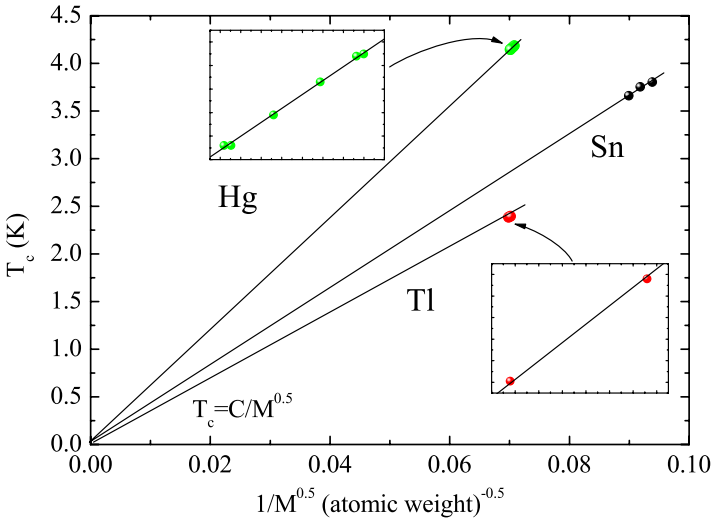

Figure 1. The superconducting critical temperature T_c of three metallic superconductors as a function of the inverse root of their mass [1]. The solid lines are straight. The insets are magnified view of the data.

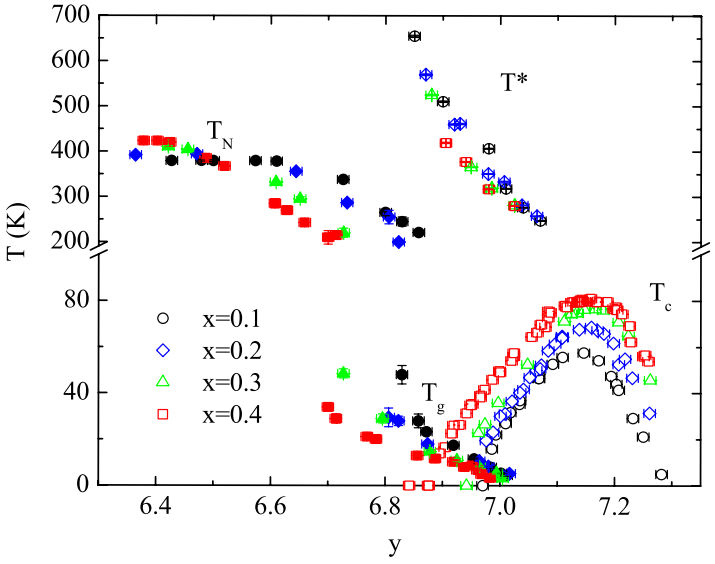

Figure 2. The phase diagram of the $(Ca_xLa_{1-x})(Ba_{1.75-x}La_{0.25+x})Cu_3O_y$ system showing the Néel (T_N), glass (T_g), superconducting (T_c) and PG (T^*) temperatures over the full doping range.

2. Main results

The phase diagram of CLBLCO including T_N, T_g, T_c and T^* versus oxygen level y is shown in figure 2. Details of the magnetic measurements are given in appendix A and PG measurements in appendix B. In the doping region up to $y = 6.5$, the T_N curves of the different families are nearly parallel. The maximum T_N (T_N^{max}) of the $x = 0.1$ family is the lowest, and of the $x = 0.4$ family the highest. Upon further doping T_N decreases rapidly and differently, leading to a crossing point after which the $x = 0.4$ family has the lowest value of T_N, and the $x = 0.1$ family the highest. By further doping, the long-range order is replaced by an SG phase, where islands of spins freeze.

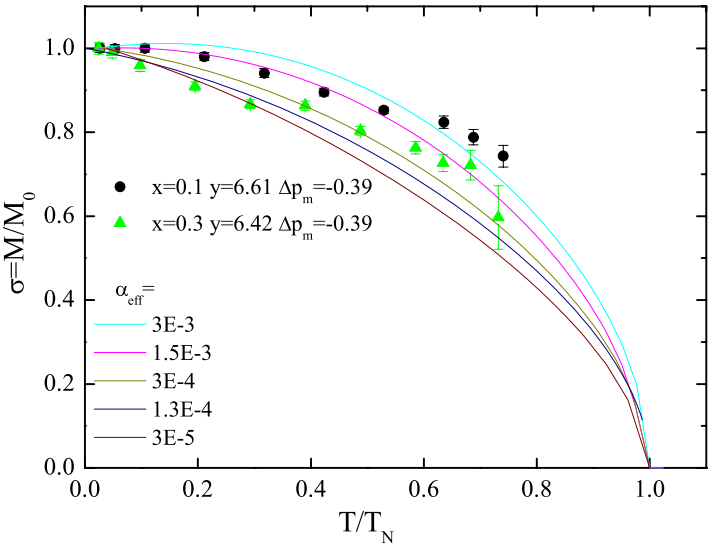

Figure 3. The normalized staggered magnetization as a function of the normalized temperature. The symbols are the experimental results for two CLBLCO samples, taken by measuring the oscillation frequency of the muon polarization curves. The parameter Δp_m is explained in the text. The solid lines are the theoretical curves for various effective anisotropic and interlayer coupling $\alpha_{eff}J$ [9].

The SG phase penetrates into the superconducting phase that exists for $y = 6.9$ to $y = 7.25$. This phase starts earlier as x increases. The superconducting domes are nearly concentric with maximum T_c (T_c^{max}) decreasing with decreasing x. T_c^{max} varies from 80 K at $x = 0.4$ to 56 K at $x = 0.1$, a nearly 30% variation. This is much stronger variation than the strongest isotope effect in nature. As for the PG temperatures T^*, it seems that the $x = 0.1$ family has the highest T^* and the $x = 0.4$ the lowest.

Perhaps the clearest feature of this phase diagram is the correlation between T_N^{max} and T_c^{max}. The family with the highest T_N^{max} has the highest T_c^{max}. However, T_N is not a clean energy scale. It is well established that a pure two-dimensional (2D) AFM orders magnetically only at $T = 0$, and that T_N is finite only for 3D AFM. Intermediate cases are described by more complicated interactions where J is the isotropic Heisenberg interaction, and $\alpha_{eff}J$ represent interlayer and anisotropic coupling [5]. In order to extract J from T_N, α_{eff} must be determined.

One method of extracting α_{eff} is from the magnetic order parameter M versus temperature T [5, 16]. For small α_{eff}, the reduction of the magnetic order parameter M with increasing T is fast so that at $\alpha_{eff} = 0$ the 2D limit is recovered. On the other hand, in the 3D case, where $\alpha_{eff} = 1$, we expect a weak temperature dependence of M at $T \to 0$ due to lack of antiferromagnetic magnon states at low frequencies. A plot of the normalized order parameter $\sigma = M/M_0$, where M_0 is the order parameter at $T \to 0$, versus T/T_N should connect (1, 0) to (0, 1) as depicted in figure 3 [9]. The differences between curves are set only by α_{eff} and they can be fitted to experimental data. Given α_{eff} and T_N, J can be extracted. This is not a very accurate method of α_{eff} determination, but J depends only on $\ln(\alpha_{eff})$ so high accuracy is not required [5].

Using zero field muon spin rotation, we determined the muon angular rotation frequencies ω in the different compounds [9]. The normalized order parameter is given by

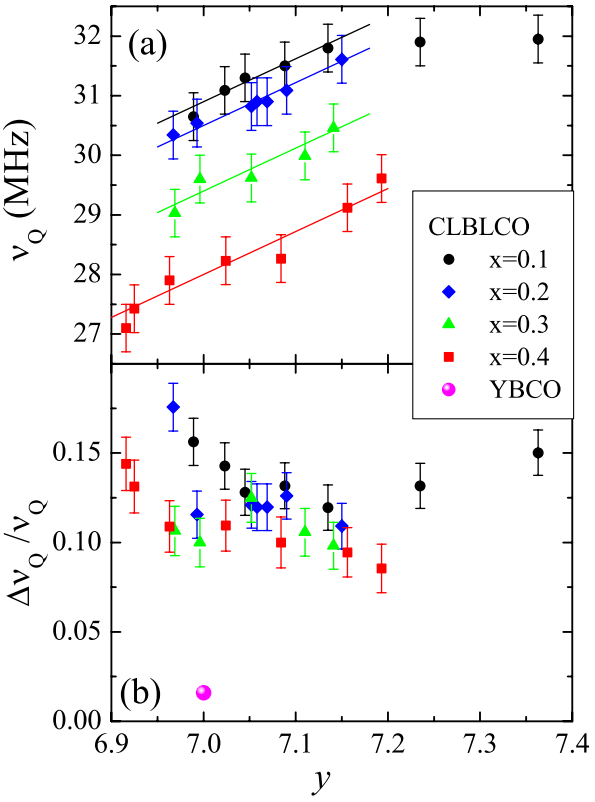

Figure 4. Nuclear quadrupole resonance frequency (a) and the line width of the in plane ^{63}Cu(2) (b) in all the CLBLCO samples extracted from NMR spectra [10]. Data for $YBa_2Cu_3O_7$ are also shown.

$\sigma(T) = \omega(T)/\omega(0)$. The order parameter extracted from the high angular frequency, around a few tens of Mrad s^{-1} ($\omega \sim 27$ Mrad s^{-1} in our case), is known to agree with neutron scattering determination of σ.

In figure 3, we also present σ for two different underdoped CLBLCO samples with $x = 0.1$ and 0.3. Clearly the reduction of the magnetization with increasing temperature is not the same for these two samples, and therefore their anisotropies are different. Since σ is less sensitive to increasing T in the $x = 0.1$ family than in the $x = 0.3$ family, the α_{eff} of $x = 0.1$ must be larger. Using the muon spin rotation frequency versus T and calculations based on the Schwinger boson mean field (SBMF) theory [5, 9], we determined α_{eff} for all samples [9]. Knowing T_N and α_{eff} for all samples, we extract a corrected T_N (T_N^{cor}). For the very underdoped samples, this $T_N^{\text{cor}} = J$. For doped samples, the situation is more complicated since the samples are described more accurately by the t–J model. We will present T_N^{cor} shortly after discussing the doping.

Doping in CLBLCO is done by controlling the oxygen level in a chain layer as in YBCO. This leaves some ambiguity concerning the doping of the CuO_2 planes. One possibility to determine the amount of charge present in this plane is to measure the in-plane Cu NQR frequency ν_Q. Assuming the lattice parameters variations within a family can be ignored (an assumption tested with neutrons in appendix E) the NQR frequency is proportional to the level of doping in the plane. The in-plane Cu NQR frequencies, discussed further in appendix C, are shown in figure 4(a). It is clear that ν_Q grows linearly with doping in the underdoped side

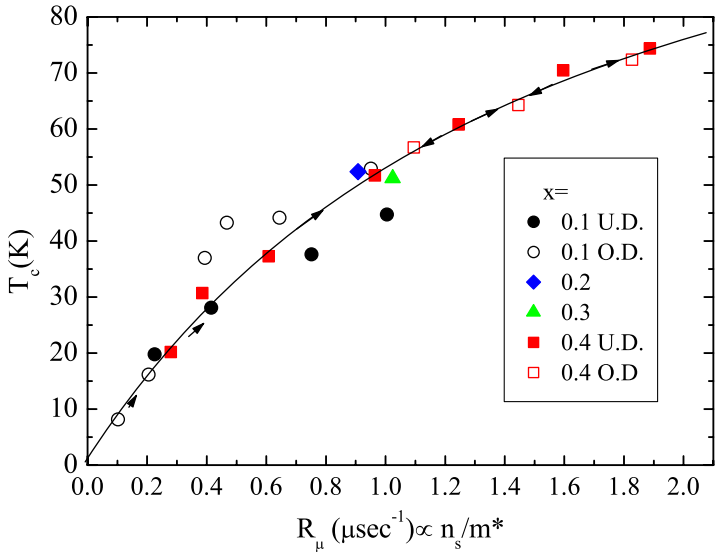

Figure 5. An Uemura plot showing T_c versus the muon relaxation rate R_μ expected to be proportional to the superconducting carrier density n_s over the effective mass m^* for the CLBLCO family of superconductors.

of the phase diagram. The most interesting finding is that, within the experimental error, the slope of $\nu_Q(x, y)$ in the underdoped side is x-independent, as demonstrated by the parallel solid lines. This means that the rate at which holes p are introduced into the CuO_2 planes, $\partial p/\partial y$, is a constant independent of x or y in the underdoped region. Using further the ubiquitous assumption that the optimal hole density, at optimal oxygenation, y_{opt}, is universal, we conclude that the in-plane hole density is a function only of $\Delta y = y - y_{opt}$. The same conclusion was reached by x-ray absorption spectroscopy (XAS) experiments [17].

In contrast, the CLBLCO family obeys the Uemura relations in the entire doping region, namely, T_c is proportional to n_s/m^*, where n_s is the superconducting carrier density and m^* the effective mass [11]. This is determined with transverse field μSR measurements where the Gaussian relaxation rate R_μ is proportional to n_s/m^* as explained in appendix D [18, 19]. The experimental results are depicted in figure 5 for all families. This experiment seems to contradict the NQR results for the following reason. If all holes had turned superconducting ($p = n_s$), then samples of different x but identical Δy should have identical Δp and identical Δn_s. In addition, if m^* is universal, samples with a common Δy should have the same T_c, in contrast to the phase diagram of figure 2. Something must be wrong in the hole counting. A similar conclusion was reached in the investigation of $Y_{1-x}Ca_xBa_2Cu_3O_{6+y}$ [20].

This problem can be solved by assuming that not all holes are mobile and turn superconducting. Therefore, we should define the mobile hole concentration Δp_m by multiplying Δy by a different constant per family $K(x)$, namely, $\Delta p_m = K(x)\Delta y$. The superconducting carrier density variation Δn_s is now proportional to Δp_m with a universal factor. The Ks are chosen so that the superconducting critical temperature T_c domes, normalized by T_c^{max} of each family, collapse onto each other. This is shown in figure 6(a) using $K = 0.76$, 0.67, 0.54, 0.47 for $x = 0.1, \ldots, 0.4$. An animation showing the rescaling of the critical temperatures and doping is available from stacks.iop.org/NJP/11/065006/mmedia.

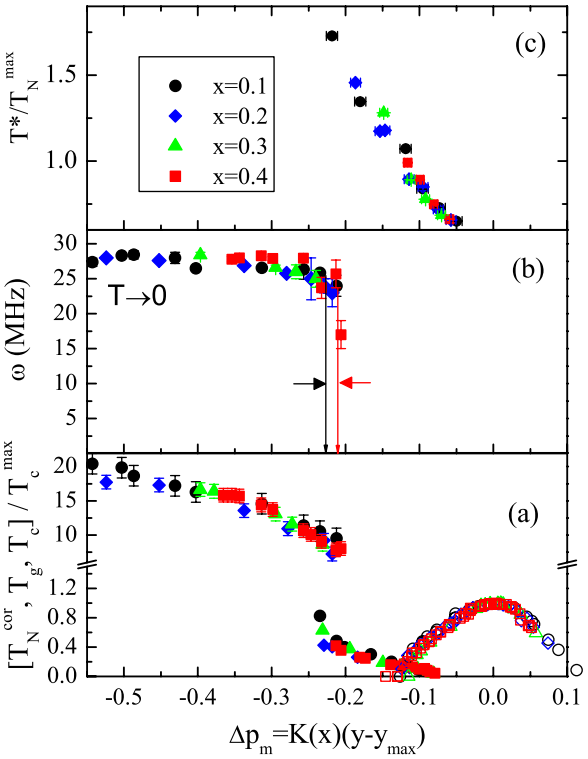

Figure 6. Unified phase diagram of CLBLCO including several experimental parameters plotted as a function of mobile hole variation Δp_{m} as described in the text: (a) superconducting critical temperature T_{c}, the SG temperature T_{g} and the corrected Néel temperature $T_{\mathrm{N}}^{\mathrm{cor}}$, which is identical to the Heisenberg superexchange J at zero doping. All parameters are normalized by $T_{\mathrm{c}}^{\mathrm{max}}$ of each family. (b) The zero temperature muon oscillation frequency equivalent to the magnetic order parameter, for all four CLBLCO families. The vertical lines show the expected difference in the critical doping had it varied by 5% between families. (c) The PG temperature normalized by the maximum Néel temperature (see text) $T^*/T_{\mathrm{N}}^{\mathrm{max}}$.

Figure 6(a) also shows the other critical temperatures $T_{\mathrm{N}}^{\mathrm{cor}}$ and T_{g} normalized by $T_{\mathrm{c}}^{\mathrm{max}}$ and plotted as a function of Δp_{m}. The critical temperatures from all families collapse to a single function of Δp_{m}. This means that there is proportionality between the in-plane Heisenberg coupling constant J and the maximum of the superconducting transition temperature $T_{\mathrm{c}}^{\mathrm{max}}$ in the series of $(\mathrm{Ca}_x\mathrm{La}_{1-x})(\mathrm{Ba}_{1.75-x}\mathrm{La}_{0.25+x})\mathrm{Cu}_3\mathrm{O}_y$ families. In fact, the data presented up to here can be explained by replacing the $1/m^*$ in the Uemura relation by a family-dependent magnetic energy scale J_x and writing

$$T_{\mathrm{c}} = cJ_x n_{\mathrm{s}}(\Delta y), \tag{1}$$

where c is a universal constant for all families. For a typical superconductor having $T_{\mathrm{c}} = 80\,\mathrm{K}$, $J \sim 1000\,\mathrm{K}$, and 8% superconducting carrier density per Cu site, c is of the order of unity. This is the main finding of this paper. Theoretical indications for the importance of J and n_{s} in setting up T_{c} could be found since the early days of HTSC [3].

Having established a proportionality between T_{c} and J, it is important to understand the origin of the J variations between families in CLBLCO. As we show in appendix E using lattice

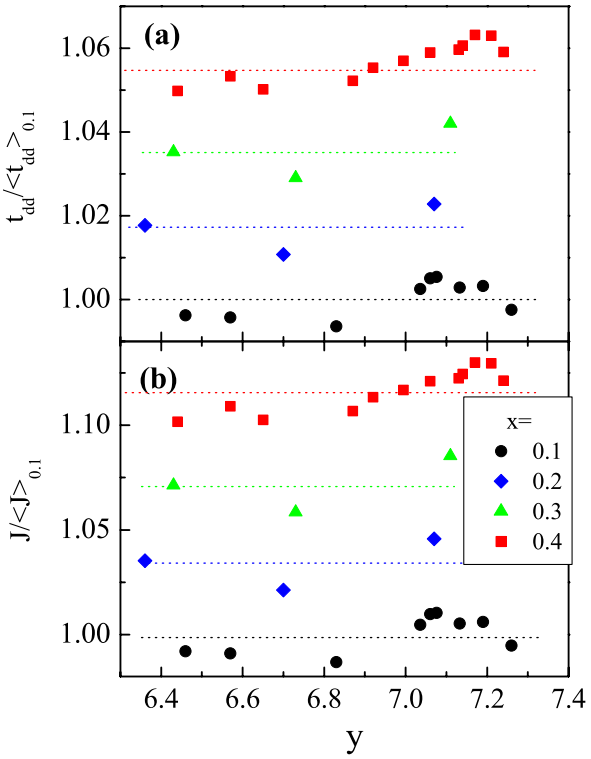

Figure 7. The hopping rate t_{dd} (a) and the superexchange coupling J (b) obtained from crystal structure data and the approximations $t_{dd} \propto \cos\theta/a^{-7}$ and $J \propto t_{dd}^2$, where θ is the buckling angle and a is the bond length shown in figure E.1.

parameter measurements with neutron diffraction, the Cu–O–Cu buckling angle is responsible for these J variations since it is the only lattice parameter that shows strong differences between the families; there is about 30% change from the $x = 0.1$ family to $x = 0.4$ [12]. This change is expected since as x increases, a positive charge is moving from the Y to the Ba site of the YBCO structure, pulling the oxygen toward the plane and flattening the Cu–O–Cu bond.

From the lattice parameters it is possible to construct the hopping integral t and J of the t–J model, assuming that the Hubbard U and the charge transfer energy Δ are family-independent. The basic quantity is the hopping integral t_{pd} between Cu $3d_{x^2-y^2}$ and O 2p orbitals [21]. This hopping integral is proportional to bond length a to the power -3.5 [22]. The hopping from the O 2p to the next Cu $3d_{x^2-y^2}$ involves again the bond length and cosine of the buckling angle θ. Thus, the Cu to Cu hopping depends on a and θ as $t_{dd} \propto \cos\theta/a^{-7}$ and J is proportional to t_{dd}^2, hence, $J \propto \cos^2\theta/a^{14}$.

Estimates of the t_{dd} and J, normalized to the averaged values of the $x = 0.1$ family, $\langle t_{dd}\rangle_{0.1}$ and $\langle J\rangle_{0.1}$, are presented in figures 7(a) and (b). Although there is a variation in t and J within each family, the variation is much larger between the families. J increases with increasing x, in qualitative agreement with experimental determination of J. There is a 10% increase in J, which is *not* big enough to explain the variations in T_N^{cor}, but the magnitude and direction are satisfactory. More accurate calculations are on their way [23]. It is also important to note that there is about 5% difference in the t/J ratio between the two extreme families.

Equally important is to understand what is not changing between families. For example, we would like to check whether the crystal quality is the same for all families. Figure 4(b) shows

the width of the NQR lines discussed in appendix C [10]. This width is minimal at optimal doping and is identical within experimental resolution for all families. More recent experiments with oxygen 17 lines, and better resolution, provide the same conclusions [24]. A third piece of evidence for the similarity of crystal quality comes from XAS [25]. Thus, the variations in T_c for the different families cannot be explained by disorder or impurities.

The unified phase diagram in figure 6(a) reveals more information about the CLBLCO family than just equation (1). In particular, the fact that the Néel order is destroyed for all families at the same critical Δp_m is very significant. The disappearance of the long-range Néel order and its replacement with a glassy ground state could be studied more clearly by following the order parameter as a function of doping. Naturally, $\omega(T \to 0)$ disappears (drops to zero) only when the Néel order is replaced by the SG phase as seen in figure 6(b). We found that the order parameter is universal for all families, and, in particular, the critical doping is family-independent [12]. To demonstrate this point we show, using the two arrows in figure 6(b), what should have been the difference in the critical doping had it changed between the $x = 0.4$ and $x = 0.1$ by 5% of the doping from zero, namely, 5% of $\Delta p_m = 0.3$. Our data indicate that $M_0(\Delta p_m)$ is family-independent to better than 5%. This is a surprising result considering the fact that t/J varies between families by more than 5% and that the critical doping is expected to depend on t/J [26]. A possible explanation is that the destruction of the AFM order parameter should be described by a hopping of boson pairs, where t is absorbed into the creation of tightly bound bosons leaving a prominent energy scale J [27]. The proximity of the magnetic critical doping to superconductivity makes this possibility appealing.

Finally, we discuss the scaling of the PG temperature. T^* determined by magnetization measurements (see appendix B) behaves like the well-known PG or the spin gap measured by other techniques on a variety of superconductor samples [28]. More importantly, a small but clear family dependence of T^* is seen. At first glance in figure 2, it appears that T^* has anti-correlation with T_c^{max} or the maximum T_N (T_N^{max}). The $x = 0.4$ family, which has the highest T_c^{max} and T_N^{max}, has the lowest T^*, and vice versa for the $x = 0.1$ family.

However, this conclusion is reversed if instead of plotting the T^* as a function of oxygen level, it is normalized by T_N^{max}, and plotted as a function of mobile hole variation Δp_m [13]. This is demonstrated in figure 6(c). Here T_N^{max} are chosen so that the $T_N(\Delta p_m)/T_N^{max}$ curves collapse onto each other, and are 379, 391.5, 410 and 423 K for the $x = 0.1, \ldots, 0.4$ families, respectively. Therefore, T_N^{max} should be interpreted as the extrapolation of T_N to the lowest Δp_m. Normalizing T^* by T_c^{max} does not provide as good data collapse as the normalization by T_N^{max} [13]. We conclude that a PG does exist in CLBLCO and that it scales with the maximum Néel temperature of each family. Therefore, the PG is a 3D phenomenon involving both in- and out of-plane coupling. A similar conclusion was reached by resistivity analysis [14] and theoretical considerations [15].

3. Conclusions

In this work, four families of cuprate superconductors with a maximum T_c variation of 30% are investigated. It is demonstrated experimentally that these families are nearly identical in their crystal structure and crystal quality. The only detectable property that varies considerably between them is the Cu–O–Cu buckling angle. This angle is expected to impact the holes hopping rate t, hence, the magnetic superexchange J between Cu spins. J in turn sets the scale for the Néel temperature where long-range antiferromagnetic order is taking place. Independent

measurements of J show that indeed J varies between families and that T_c grows when J increases. A linear transformation from oxygen concentration to mobile hole concentration can generate a unified phase diagram in which T_c is in fact proportional to J for all doping. Since T_c is also proportional to the superconducting carrier density it obeys equation (1).

Surprisingly, the critical density, where the Néel order is destroyed at zero temperature upon doping, is identical for all families. The critical doping is expected to depend on t/J. This result has two implications. On the one hand it supports the validity of the linear doping transformation; on the other hand, it suggests that this transformation has eliminated t from the low temperature effective Hamiltonian.

Finally, it is found that the PG temperature T^*, as measured by susceptibility, scales better with the Néel temperature than with J (or T_c). This suggests that T^* is determined by both in- and out-of-plane coupling, and should be viewed as a temperature where the system attempts unsuccessfully to order magnetically.

Acknowledgments

The author acknowledges very helpful discussions with A Kanigel, R Ofer, E Amit, A Auerbach, Y J Uemura and H Alloul. Financial support from the Israel Science Foundation is also acknowledged.

Appendix A. Magnetic critical temperatures

The Néel and SG temperatures presented in figures 2, 3 and 6 are obtained by zero field μSR. In these experiments, we determine the time-dependent spin polarization $P_z(t)$ of a muon injected into the sample at different temperatures. z represents the initial muon spin direction. Figure A.1 shows typical $P_z(t)$ curves, at different temperatures, for three samples from the $x = 0.1$ family. At high temperatures, the polarization curves from all samples are typical of magnetic fields emanating from nuclear magnetic moments. In this case, the time-dependence of the polarization exhibits a Gaussian decay. As the temperature is lowered, the sample enters a magnetic frozen phase and the polarization relaxes much more rapidly. While the transition from the paramagnetic to the frozen state looks identical for all samples, the behavior at very low T is different and indicates the nature of the ground state. Figure A.1(a) is an example of an antiferromagnetic ground state. When the temperature decreases, long-range magnetic order is established at ~ 377 K reflected by spontaneous oscillations of $P(t)$.

Figure A.1(c) is an example of an SG transition at ~ 17 K. In this case, the ground state consists of magnetic islands with randomly frozen electronic moments [8], and consequently the polarization shows only rapid relaxation. When the transition is to a Néel or SG state, the critical temperatures are named T_N and T_g, respectively. Figure A.1(b) presents an intermediate case where the sample appears to have two transitions. The first one starts below 240 K, where the fast decay in the polarization appears. Between 160 and 40 K there is hardly any change in the polarization decay, and at 30 K there is another transition manifested in a faster decaying polarization. This behavior was observed in all the samples on the border between AFM and spin-glass in the phase diagram.

In order to determine the magnetic critical transition temperatures, the data were fitted to a sum of two functions: a Gaussian with amplitude A_n representing the normal fraction of

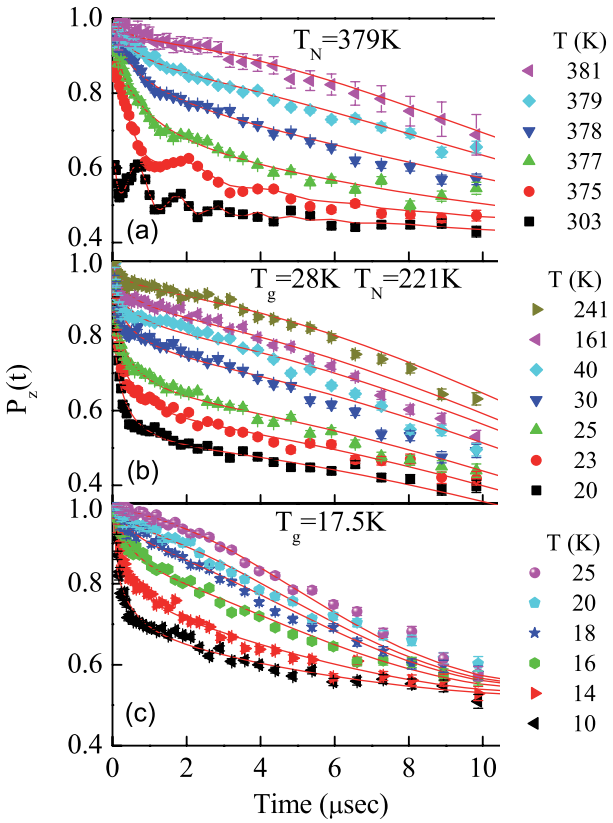

Figure A.1. Time evolution of the muon polarization for the $x = 0.1$ family close to the magnetic critical temperature. (a) A sample with an AFM transition. (b) A sample with both an AFM and an SG transition. (c) A sample with an SG transition. The solid lines are a fit as described in the text.

the sample, and a rapidly relaxing and oscillating function, with amplitude A_m and angular frequency ω, representing the magnetic fraction and describes the magnetic field due to frozen electronic moments [9, 12]. In this function, the sum $A_m + A_n = 1$ is constant at all temperatures. Figure A.2 shows A_m as a function of temperature, for the three samples in figure A.1. Above the transition, where only nuclear moments contribute, A_m is close to zero. As the temperature decreases, the frozen magnetic part increases and so does A_m, at the expense of A_n. For the pure AFM and SG phases, the transition temperature was determined as the temperature at which A_m is half of the saturation value. For the samples with two transitions, two temperatures were determined using the same principle.

The magnetic order parameter is extracted from the muon rotation frequency in zero field as seen in figure A.1(a). These rotations allow us to determine $\omega(T, x, y)$. The temperature dependence of ω is used to determine the effective interlayer and anisotropic interaction α_{eff} in figure 3. $\omega(0, x, y)$ is used to determine the family-dependent critical doping in figure 6(b).

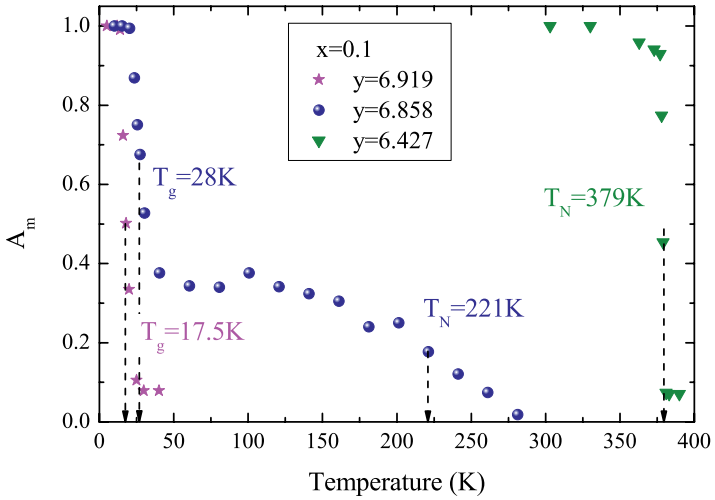

Figure A.2. The magnetic amplitude fraction A_{m} extracted from the muon depolarization as a function of temperature for the three samples shown in figure A.1.

Appendix B. Pseudogap

We determine T^* using temperature-dependent magnetization measurements. In figure B.1(a), we present raw data from four samples of the $x = 0.2$ family with different doping levels. At first glance, the data contain only two features: a Curie–Weiss (CW) type increase of χ at low temperatures, and a non-zero baseline at high temperature (~ 300 K). This base line increases with increasing y. The CW term is very interesting but will not be discussed further here. The baseline shift could be a consequence of variations in the core and Van Vleck electron contribution or an increasing density of states at the Fermi level.

A zoom-in on the high-temperature region, marked by the ellipse, reveals a third feature in the data: a minimum point of χ. To present this minimum clearly, we subtracted from the raw data the minimal value of the susceptibility χ_{min} for each sample and plotted the result on a tighter scale in figure B.1(b). The χ minimum is a result of decreasing susceptibility upon cooling from room temperature, followed by an increase in the susceptibility due to the CW term at low T. This phenomenon was previously noticed by Johnston *et al* in YBCO [29], and Johnston [30] and Nakano *et al* [31] in $La_{2-x}Sr_xCuO_4$ (LSCO). The minimum point moves to higher temperatures with decreasing oxygen level as expected from T^*. There are three possible reasons for this decreasing susceptibility: (i) increasing AFM correlations upon cooling, (ii) opening of an SG where excitations move from $q = 0$ to the AFM wavevector [32], or (iii) disappearing density of states at the Fermi level as parts of the Fermi arc are being gapped out when the PG opens as T/T^* decreases [33].

In order to determine the T^*, we fit the data to a three-component function $\chi = C_1/(T + \theta) + C_2\tanh(T^*/T) + C_3$. The fits are presented by solid lines in figure B.1. The values of T^* are shown in figures 2 and 6.

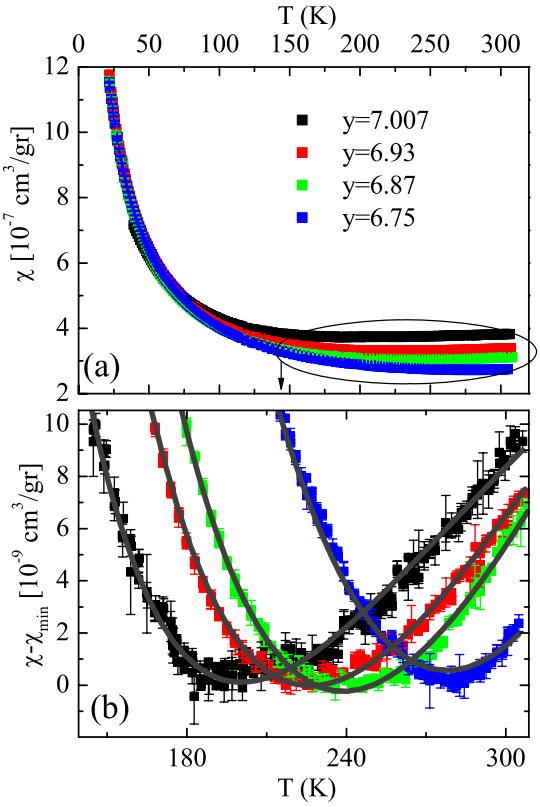

Figure B.1. Raw susceptibility data from four samples of the $x = 0.2$ family with different doping levels (a). Zoom-in on the data in the ellipse of (a) after the minimum value of χ is subtracted (b). The solid lines are fits described in the text.

Appendix C. Doping and impurities

The Cu-NQR experiment is done on powder samples fully enriched with ^{63}Cu. We measured between five and seven different samples for each x in the normal state at 100 K. The most overdoped sample is a non superconducting $x = 0.1$ compound. The NMR measurements were done by sweeping the field in a constant applied frequency $f_{\text{app}} = 77.95$ MHz, using a $\pi/2$–π echo sequence. The echo signal was averaged 100 000 times and its area evaluated as a function of field. The data are presented in figure C.1. The full spectrum of the optimally doped $x = 0.4$ sample ($y = 7.156$) is shown in the inset of figure C.1. The main planes emphasize the important parts of the spectrum using three axis breakers.

The evolution of the main peaks as x increases is highlighted by the dotted lines. It is clear that as x decreases the peaks move away from each other. This means that ν_Q at optimal doping is a decreasing function of x. A more interesting observation is the fact that there is no change in the width of the peaks, at least not one that can easily be spotted by the naked eye. This means that the distribution of ν_Q is x-independent and that there is no difference in the disorder between the optimally doped samples of the different families. Thus, as mentioned in section 2,

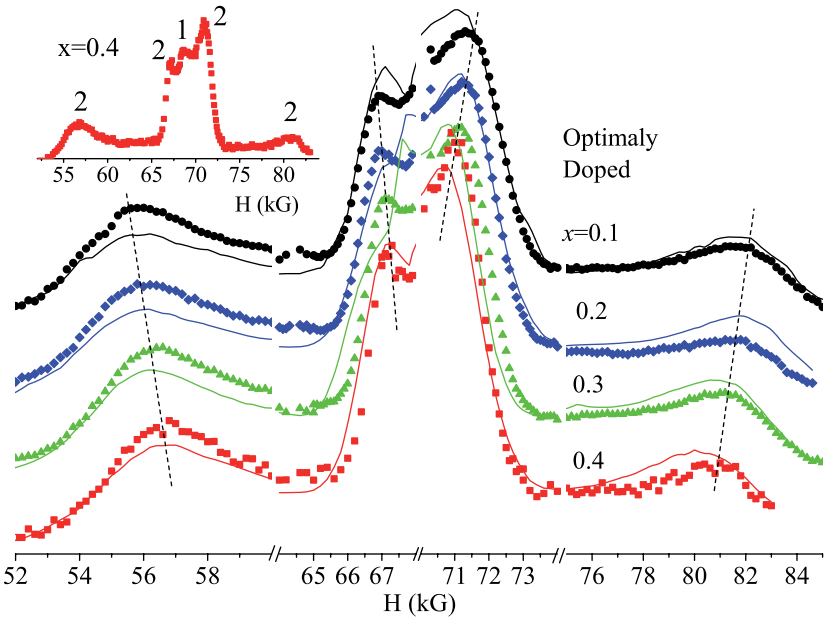

Figure C.1. NMR spectra of ^{63}Cu at $T = 100$ K in optimally doped CLBLCO samples with varying x. The inset shows the full spectrum of the $x = 0.4$ compound including contributions from the chain copper Cu(1) and plane copper Cu(2). The main figure zooms in on the Cu(2) contribution (note the three axis breakers). The positions of the Cu(2) peaks are shown by dotted lines. The solid lines are fits to NQR line shape, from which ν_Q and $\Delta\nu_Q$ of figure 4 are obtained [10].

disorder is not relevant to the variation of T_c^{max} between the different families. This conclusion is supported by more rigorous analysis [10]. ν_Q and $\Delta\nu_Q$ presented in figure 4 are obtained by fitting NQR line shape to these data as demonstrated by the solid lines.

Appendix D. Penetration depth

The penetration depth is measured with transverse field TF-μSR. In this experiment, one follows the transverse muon polarization $P_\perp(0)$ when a magnetic field is on and perpendicular to the initial polarization. These experiments are done by field cooling (FC) the sample to 1.8 K at an external field of 3 kOe. Every muon precesses according to the local field in its environment. When FC the sample, a vortex lattice is formed, and the field from these vortices decays on a length scale of the penetration depth λ. This leads to an inhomogeneous field distribution in the sample. Since the magnetic length scale is much larger than the atomic one, the muons probe the magnetic field distribution randomly, which, in turn, leads to a damping of the muons average spin polarization. This situation is demonstrated in figure D.1, where we present $P_\perp(0)$ in two different perpendicular directions (called real and imaginary) in a rotating reference frame. At temperatures above T_c, the field is homogeneous and all muons experience the same field, and therefore no relaxation is observed. Well below T_c (of 77 K in this case) there are strong field variations and therefore different muons precess with different frequencies, and the average polarization quickly decays to zero. At intermediate temperatures, the field variation is not severe and the relaxation is moderate.

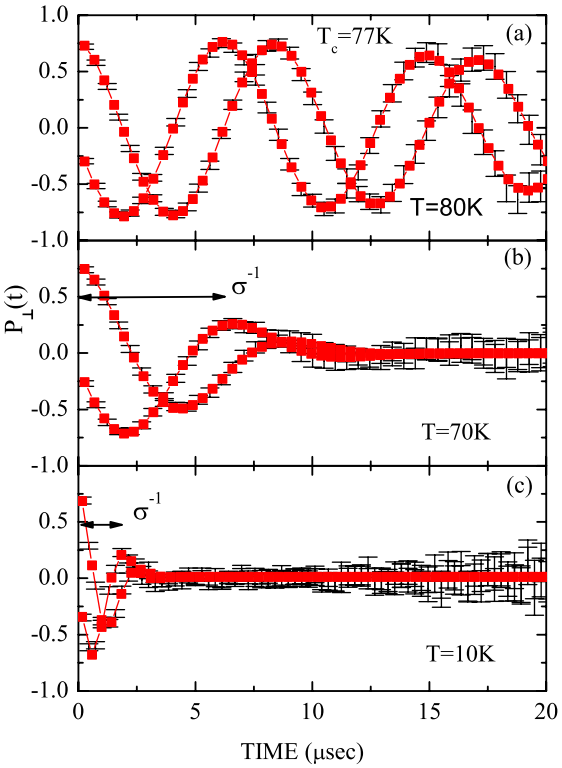

Figure D.1. Demonstrating the real and imaginary polarization in a TF-μSR experiment as the temperature is lowered below T_c. The data are presented in a rotating reference frame.

It was shown that in powder samples of HTSC the muon polarization $P_\perp(t)$ is well described by $P_\perp(t) = \exp(-R_\mu^2 t^2/2)\cos(\omega t)$, where $\omega = \gamma\mu H$ is the precession frequency of the muon, and R_μ is the relaxation rate [18]. The solid line in this figure is the fit result. The fact that the whole asymmetry relaxes indicates that CLBLCO is a bulk superconductor. The fit results for R_μ are shown in figure 5. As can be seen, the dependence of T_c on R_μ is linear in the under-doped region and universal for all CLBLCO families, as expected from the Uemura relations. However, there is a new aspect in this plot. There is no 'boomerang' effect, namely, overdoped and underdoped samples with equal T_c have the same R_μ, with only slight deviations for the $x = 0.1$. Therefore, in CLBLCO there is one to one correspondence between T_c and R_μ, and therefore n_s/m^*, over the whole doping range.

Appendix E. Lattice parameters

Neutron powder diffraction experiments were performed at the Special Environment Powder Diffractometer at Argonne's Intense Pulsed Neutron Source (see [34] for more details). Figure E.1 shows a summary of the lattice parameters. The empty symbols represent data taken from [34]. All the parameters are family-dependent, but not to the same extent. The lattice parameters a and c, depicted in figures E.1(a) and (b), change by up to about 0.5% between the two extreme families ($x = 0.1$ and $x = 0.4$). The in-plane Cu–O–Cu buckling angle is shown in

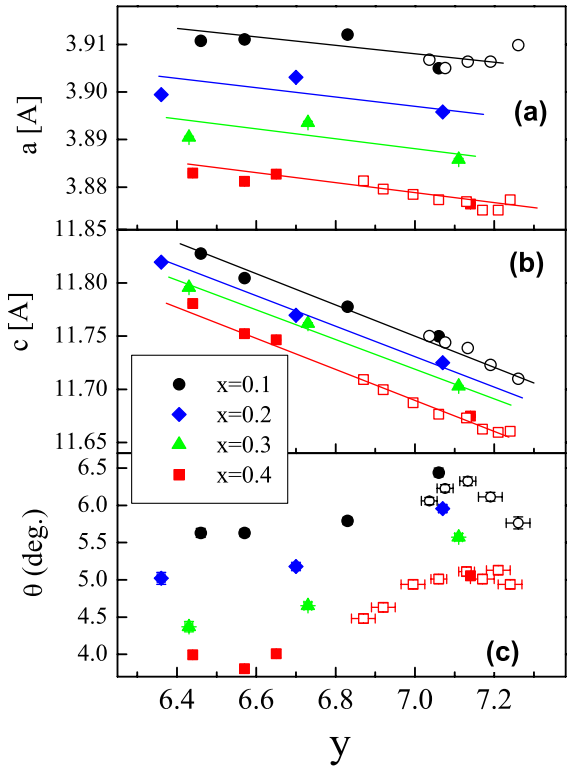

Figure E.1. Lattice parameters as a function of oxygen doping. (a) The lattice parameter a. (b) The lattice parameter c. (c) θ, the buckling angle between the copper and oxygen in the plane. The empty symbols are from [34]. The lines are guides to the eye.

figure E.1(c). This angle is non-zero since the oxygen is slightly out of the Cu plane and closer to the Y site of the YBCO structure. As mentioned in section 2, it changes by 30% between families.

References

[1] Reynolds C A *et al* 1950 *Phys. Rev.* **84** 691
Serin B *et al* 1952 *Phys. Rev.* **86** 162
Maxwell E and Lutes O S 1954 *Phys. Rev.* **95** 333
[2] Scalapino D 1995 *Phys. Rep.* **250** 329
Chubukov A V, Pines D and Stojković B P 1996 *J. Phys.: Condens. Matter* **8** 10017
Altman E and Auerbach A 2002 *Phys. Rev.* B **65** 104508
Muñoz D, Moreira de P R and Illas F 2002 *Phys. Rev.* B **65** 224521
Anderson P W, Lee P A, Randeria M, Rice T M, Trivedi N and Zhang F C 2004 *J. Phys.: Condens. Matter* **16** R755
Demler E, Hanke W and Zhang S-C 2004 *Rev. Mod. Phys.* **76** 909
Kivelson S A and Fradkin E 2005 arXiv:cond-mat/0507459
Moriya T and Ueda K 2003 *Rep. Prog. Phys.* **66** 1299

[3] Kotliar G 1988 *Phys. Rev.* B **37** 3664
Kancharla S S, Kyung B, Sénéchal D, Civelli M, Capone M, Kotliar G and Tremblay A-M S 2008 *Phys. Rev.* B **77** 184516
[4] Tranquada J M, Shirane G, Keimer B, Shamoto S and Sato M 1989 *Phys. Rev.* B **40** 4503
Preyer N W *et al* 1988 *Phys. Rev.* B **37** 9761
[5] Keimer B *et al* 1992 *Phys. Rev.* B **54** 7430
[6] Wan X, Majer T A and Savrasov S Y 2009 *Phys. Rev.* B **79** 155114
[7] Goldschmidt D, Reisner G M, Direktovitch Y, Knizhnik A, Gartstein E, Kimmel G and Eckstein Y 1993 *Phys. Rev.* B **48** 532
[8] Kanigel A, Keren A, Eckstein Y, Knizhnik A, Lord J S and Amato A 2002 *Phys. Rev. Lett.* **88** 137003
[9] Ofer R, Bazalitsky G, Kanigel A, Keren A, Auerbach A, Lord J S and Amato A 2006 *Phys. Rev.* B **74** 220508
[10] Keren A, Kanigel A and Bazalitsky G 2006 *Phys. Rev.* B **74** 172506
[11] Keren A, Kanigel A, Lord J S and Amato A 2003 *Solid State Commun.* **126** 39
[12] Ofer R, Keren A, Chmaissem O and Amato A 2008 *Phys. Rev.* B **78** 140508
[13] Lubashevsky Y and Keren A 2008 *Phys. Rev.* B **78** 020505
[14] Su Y H, Luo H G and Xiang T 2006 *Phys. Rev.* B **73** 134510
[15] Millis A J and Monien H 1993 *Phys. Rev. Lett.* **70** 2810
[16] Arovas D P and Auerbach A 1998 *Phys. Rev.* B **38** 316
[17] Sanna S, Agrestini S, Zheng K, Saini N L and Bianconi A, in preparation
[18] Lee S L, Kilcoyne S H and Cywinski R (ed) 1999 *Muon Science: Muons in Physics, Chemistry and Materials* (London: Institute of Physics)
[19] Sonier J E 2007 *Rep. Prog. Phys.* **70**
[20] Sanna S, Coneri F, Rigoldi A, Concas G and De Renzi R 2008 *Phys. Rev.* B **77** 224511
[21] Zaaneann J and Sawatzky D G A 1987 *Can. J. Phys.* **65** 1262
[22] Harrison W A 1980 *Electronic Structure and the Properties of Solids* (San Francisco, CA: Freeman)
[23] Petit S and Lepetit M-B, in preparation
[24] Amit E and Keren A, in preparation
[25] Sanna S 2007 private communication
[26] Khaliullin G and Horsch P 1993 *Phys. Rev.* B **47** 463
Belkasri A and Richard J L 1994 *Phys. Rev.* B **50** 12896
Richard J L and Yushankha V Yu 1994 *Phys. Rev.* B **50** 12927
Yamamoto D and Kurihara S 2007 *Phys. Rev.* B **75** 134520
[27] Havilio M and Auerbach A 1999 *Phys. Rev. Lett.* **83** 4848
[28] Timusk T and Statt B 1999 *Rep. Prog. Phys.* **62** 61
Norman M R, Pines D and Kallin C 2005 *Adv. Phys.* **54** 715
Lee P A, Nagaosa N and Wen X-G 2006 *Rev. Mod. Phys.* **78** 17
[29] Johnston D C *et al* 1987 *Chemistry of High-Temperature Superconductors* (Washington, DC: American Chemical Society) p 149
[30] Johnston D C 1989 *Phys. Rev. Lett.* **62** 957
[31] Nakano T, Oda M, Manabe C, Momono N, Miura Y and Ido M 1994 *Phys. Rev.* B **49** 16000
[32] Rossat-Mignod J *et al* 1992 *Physica* B **180–181** 383
Regnault L P *et al* 1995 *Physica* C **235** 59
Julien M-H *et al* 1996 *Phys. Rev. Lett.* **76** 4238
[33] Kanigel A *et al* 2006 *Nat. Phys.* **2** 447
[34] Chmaissem O, Jorgensen J D, Short S, Knizhnik A, Eckstein Y and Shaked H 1999 *Nature* **397** 45